Comparison of an analog direct detection and a micropulse aerosol lidar at 1.5-μm wavelength for wind field observations—with first results over the ocean

Shane D. Mayor
Pierre Dérian
Christopher F. Mauzey
Scott M. Spuler
Patrick Ponsardin
Jeff Pruitt
Darrell Ramsey
Noah S. Higdon

Comparison of an analog direct detection and a micropulse aerosol lidar at 1.5-*µ*m wavelength for wind field observations—with first results over the ocean

Shane D. Mayor,[a,*] **Pierre Dérian,**[a] **Christopher F. Mauzey,**[a]
Scott M. Spuler,[b] **Patrick Ponsardin,**[c] **Jeff Pruitt,**[c]
Darrell Ramsey,[c] **and Noah S. Higdon**[c]
[a]California State University Chico, 400 West First Street, Chico, California 95928, United States
[b]National Center for Atmospheric Research, P.O. Box 3000, Boulder,
Colorado 80307-3000, United States
[c]Spectral Sensor Solutions, LLC, 2613 Paddock Gate Court, Herndon,
Virginia 20171, United States

Abstract. The performance of two direct-detection atmospheric lidar systems with very different methods of generating and detecting laser radiation is compared as the result of a field experiment held in March 2015, in Chico, California. During the noncontinuous, 11-day test period, in which the systems operated side by side, the micropulse lidar was operated at its maximum pulse repetition frequency (15 kHz) and integrated elastic backscatter over the interpulse period of the analog direct-detection lidar (0.1 s). Operation at the high pulse repetition frequency resulted in second-trip echoes that contaminated portions of the data. The performance of the micropulse lidar varied with background brightness—as expected with a photon-counting receiver—yet showed equal or larger backscatter intensity signal-to-noise ratio throughout the experiment. Examples of wind fields and time series of wind vectors from both systems during the Chico experiment are presented. In addition, scans over the ocean that were collected by the micropulse lidar during a subsequent deployment on the northern California coast are presented. We conclude by reviewing the advantages and disadvantages of each system and make some suggestions to improve the design and performance of future systems. © *The Authors. Published by SPIE under a Creative Commons Attribution 3.0 Unported License. Distribution or reproduction of this work in whole or in part requires full attribution of the original publication, including its DOI.* [DOI: 10.1117/1.JRS.10.016031]

1 Introduction

Detection subsystems in atmospheric lidars can be divided into two broad categories: heterodyne and direct. Heterodyne detection is employed to measure minute frequency shifts of coherent backscattered radiation in order to determine the line-of-sight component of wind velocity.[1] Direct detection[2] is employed in the majority of other lidar systems and some nonheterodyne Doppler lidars.[3,4] Within the category of direct detection, there are two possibilities: analog detection and photon counting. Analog detection systems are used when the rate of arrival of backscatter photons is too large to be counted individually. They use detectors such as avalanche photodiodes (APDs) and transimpedance amplifiers to convert a flux of photons on the active area of the detector to a voltage that can be recorded by an analog-to-digital converter.

Photon-counting detection subsystems can be used when the photon arrival rate is lower than ~ 10 Ms^{-1}. Photon-counting subsystems (also known as Geiger-mode detection subsystems) may also be referred to as digital direct detection. Some lidar systems split the backscattered radiation into both analog detection and photon-counting subsystems.[5,6] In such lidars, the

analog data are used when the backscatter signal intensity is large, and the photon-counting data are used when the intensity is weak. Photomultiplier tubes (PMTs) and single-photon avalanche diodes are used in photon-counting systems.[7,8]

The choice of analog or digital detection depends on the return signal intensity, which largely depends on the transmitter pulse energy, the type of atmospheric scattering process being studied (e.g., elastic or inelastic), and the desired range of interest. Strong transmit pulse energy generally results in strong elastic backscatter intensity within the first few kilometers of range, high photon arrival rate, and requires analog detection. Weak transmit pulse energy results in weak backscatter intensity, low photon arrival rate, and requires photon counting. Because of this general division, we refer to systems employing large pulse energy and analog detection as "macropulse" and systems employing weak pulse energy and photon counting as "micropulse." Indeed, micropulse lidars often transmit with pulse energy on the order of tens to hundreds of microjoules.[9]

A well-designed macropulse elastic lidar has the advantage of receiving all the backscattered radiation necessary to observe atmospheric structure over a long path (typically a few kilometers in the horizontal direction) from a single pulse. This leads to the advantages of being able to scan rapidly and acquire data with high angular resolution without having to integrate data from multiple pulses.[10] However, macropulse lidars require lasers capable of large pulse energy. Such transmitters tend to use bulk lasers and in some cases wavelength converters. Because the pulse energy is large and the beam diameters are small (order 1 cm or less), the energy density in the transmitter may be very large. Such laser beams require the use of free-space optics, which results in the relatively large physical sizes of such devices. Finally, such transmitters are notorious for being expensive, sensitive to environmental conditions, and requiring high levels of care and maintenance.

Micropulse lidars have the advantages of employing waveguide lasers that produce low pulse energy. These lasers tend to be less expensive, more compact, and all-solid state. They are more rugged, require no liquid cooling, and use less free-space optics (i.e., more fiber-based components) and, as such, are less sensitive to environmental conditions. On the other hand, because the backscatter signal resulting from each pulse is so small, micropulse lidars require the integration of backscatter intensity over many pulses [under most conditions, the signal-to-noise ratio (SNR) improves by the square root of the number of pulses in the integration period]. Furthermore, two additional disadvantages appear. First, because the detection systems are so sensitive, background radiation becomes a significant source of noise and requires careful filtering. Second, practical limitations in pulse rate begin to appear from second trip echoes. That is while any given pulse is traversing the region of primary interest (the first few kilometers range), backscatter signal from distant clouds or hard targets from previous pulses are superimposed on and confound the signal from the most recent pulse.

In this paper, we compare the performance of the Raman-shifted eye-safe aerosol lidar (REAL, a macropulse system) with the scanning aerosol micropulse lidar—eye-safe (SAMPLE, a micropulse system) using experimental data that was collected in Chico, California, from March 9 to 20, 2015.[11] Both systems operate at the near-infrared wavelength of 1.5 μm. Of particular interest is the performance of the SAMPLE because it is new, compact, and portable. If its performance rivals that of the REAL, then it represents a possible path forward to facilitate field deployments that would not have been possible due to the size, weight, cost, and complexity of the REAL. In Sec. 5, we present highlights from subsequent deployments of the SAMPLE on the California coast that support our conclusion that this technology will be useful at observing the aerosol distribution and wind fields using motion estimation techniques over rough ocean surfaces.

2 REAL

The original National Science Foundation (NSF) REAL[12–16] at California State University Chico (several other REALs were created by ITT Corp. for the Department of Defense) provides high SNR elastic backscatter to several kilometers range from individual laser pulses. The REAL pulse energy varies slowly over time ($\pm 20\%$) and depends mostly on the age of the flashlamps

and the flashlamp voltage—and to a lesser degree, room temperature. During field operations, we are usually able to maintain 120 to 170 mJ/pulse. The transmitted pulse energy is dependent on the wavelength conversion efficiency in the Raman shifter, which depends on the fluence of the Nd:YAG pump beam. The pulse repetition frequency is 10 Hz. REALs built by ITT Corp. operate at 20 Hz.[17] No integration of backscatter signal from multiple pulses in time is required to observe atmospheric structure over a long path (typically 3 to 5 km). The REAL pulse duration is ~6 ns (corresponding to 1.8 m in length) and the receiver subsystem employs a 14-bit analog-to-digital converter operating at 100 MSPS. That results in a data point every 1.5 m in range. The combined bandwidth of the Perkin Elmer InGaAs APD (with detector active area of 200-μm diameter) and amplifier electronics is about 10 to 20 MHz (corresponding to scales of 15 to 7.5 m in range). The backscattered radiation is split into two channels on the original NSF REAL for relative polarization sensitivity.[14] The REAL has resulted in impressive aerosol imagery that can be used with motion estimation algorithms to deduce vector wind fields.[18–20] The REAL transmitter, however, is large and challenging to maintain. It places very significant limitations on the embodiment of the entire instrument, sets substantial requirements for operation, and therefore reduces deployment opportunities.

3 SAMPLE

The SAMPLE, shown in Fig. 1(a) and on the left in Fig. 2 and available through Spectral Sensor Solutions LLC, integrates a combination of commercial-off-the-shelf and custom components into a compact system. A general system schematic is shown in Fig. 1(b). The laser in the SAMPLE is a Keopsys erbium fiber laser Model KPS-BT2-PEYFA-1555-05-Col operating at approximately the same 1.5 μm wavelength as the REAL. The laser pulse energy is 300 to 500 times lower than that of the REAL, but the pulse repetition frequency is 1500 times higher. As a result, the SAMPLE transmits an average power of 5.25 W while the REAL transmits 1.2 to 1.7 W. The Keopsys laser is attached to a custom beam expander that increases the beam diameter to 10 cm for transmission into the atmosphere. That is roughly the same as the REAL beam diameter, and both beams of course must be imaged back on to their respective detectors. In the case of the REAL, it must be focused to a considerably smaller spot: the 0.2-mm diameter active area of the APD. Doing so requires a custom optical design to achieve the 0.3 mrad field of view (FOV); whereas a 0.4 mrad FOV for a 1.6-mm diameter area of the PMT in SAMPLE (64 times larger area than the APD used in the REAL) is easily accomplished with off-the-shelf optical components.

The SAMPLE receiver employs a custom 20-cm diameter telescope that is fiber-coupled to a Hamamatsu H10330-75 PMT with 10% quantum efficiency. The photon-count data were
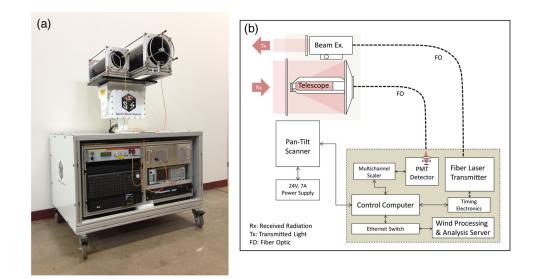

Fig. 1 (a) Photograph of the SAMPLE (summer of 2015). (b) General schematic of the SAMPLE.

Fig. 2 The SAMPLE on the left and the REAL on the right during a side-by-side comparison experiment on March 9, 2015, in Chico, California.

sampled at 20 MHz thereby providing backscatter intensity every 7.5 m in range. The PMT dark count rate is 2.5×10^5 counts s^{-1}. For the Hamamatsu PMT, the deadtime is set by the anode pulse response. This pulse is a combination of rise time, fall time, and transit time spread and is specified as 3 ns. The maximum count rate is determined by the number of shots aggregated per

Table 1 Comparison of system specifications for the REAL and the SAMPLE.

	Original NSF REAL	SAMPLE
Wavelength (μm)	1.543	1.554
Pulse rate (Hz)	10	15,000
Pulse energy (mJ)	120 to 170	0.35
Average transmit power (W)	1.2 to 1.7	5.25
Pulse duration (ns)	6	25
Pulse length (m)	1.8	7.5
Backscatter sample rate (MSPS)	100	20
Range gate spacing (m)	1.5	7.5
Transmitter type	Flashlamp-pumped Nd:YAG and Raman wavelength shifter	Pulsed fiber
Beam divergence (mrad, half angle)	0.20	0.30
Optical filter bandwidth (nm)	5	1
Detection type	Analog InGaAs APD	Photon counting PMT
Detector brand and model	Perkin Elmer C30659-1550-R2A	Hamamatsu H10330-75
Detector active area diameter (mm)	0.2	1.6
Detector quantum efficiency (%)	75	12
Telescope diameter (cm)	40	20
Receiver FOV (mrad, half angle)	0.28	0.4
Geometry	Coaxial	Biaxial
Range to full overlap (m, estimate)	500	1000
Scan mechanism	Beam steering unit	Pan/tilt positioner

histogram. For the experiment reported herein, the laser pulse repetition frequency was 15 kHz and 1500 shots were aggregated into a nominal histogram rate of 10 Hz. One-way range bins are 25 ns (set to match the pulse width of the laser) and a PMT deadtime of 3 ns produces a maximum count rate of 8 counts/range bin/shot. For 1500 shots, this is a maximum of 12,000 counts/bin.

The multichannel scaler (MCS) card is an Ortec model 9353. This MCS can resolve pulses at the 1 ns level but we use the larger 25 ns number due to the temporal pulse width of the laser. The SAMPLE includes a computer server with the same Nvidia Tesla graphical processing units and motion estimation algorithms that are used by the REAL. This gives the system the same real-time two-dimensional vector wind field sensing capability as the REAL that is described in Sec. 4.3. Properties of the REAL and the SAMPLE lidars are listed for comparison in Table 1.

Both the REAL and the SAMPLE use thin film interference filters to reduce the background radiation. A 5-nm bandwidth filter in the REAL receiver is sufficient to make the system insensitive to background radiation. The SAMPLE employs a 1-nm bandwidth filter and yet remains sensitive to background because of the single photon sensitivity of the receiver. In general, narrower filters improve performance by reducing the background signal, but the cost of custom filters narrower than 1 nm increases substantially and the bandpass should not be so narrow that it blocks any of the backscatter from the laser emission spectrum. This is potentially more of a limitation when using a pulsed fiber laser such as the one in SAMPLE where the emission spectrum may not be as narrow as that of the laser used in the REAL.

4 Experiment

The SAMPLE was deployed next to the REAL in Chico, California, from March 9 to 20, 2015. The instrument was installed in a U-Haul moving van. Figure 2 is a photograph of both systems during the experiment. The beam steering unit of the REAL and the telescope of the SAMPLE were separated by ∼10 m distance. The altitude of the site is 53 m ASL. Data for comparison were collected primarily during the day and early evening. No deliberate sources of particulate matter were created for the tests. The weather and aerosol conditions varied greatly during the 11-day experiment. The site is located in an active agricultural region with large orchards and other crops. The REAL operated continuously and the SAMPLE was operated for at least a few hours of every day of the 11-day experiment. The vast majority of scans collected were nearly horizontal plan-position-indicator (PPI) scans at an elevation angle of 2 deg above the horizon. This was done because a major objective of the program was to test the horizontal wind component estimation capability described in Sec. 4.3. Unfortunately, the SAMPLE at this time was not programmed to rapidly return the pan/tilt positioner (often referred to as the scanner) to the beginning azimuth angle after the completion of each scan (an action often referred to as "flyback"). Instead, the subsequent scan was collected in the reverse scan direction. The impact of this is uneven temporal sampling of any given point in the scan area. It makes the movement of aerosol features in the animations appear to "waddle" rather than move fluidly. This issue has no impact on our ability to compare and analyze the SNR performance of the SAMPLE with the REAL, but it does limit our ability to make fair wind field estimates resulting from the two systems.

Figure 3 shows one nearly horizontal scan (hereafter referred to as plan position indicator or PPI) from the REAL [Fig. 3(a)] and one PPI scan from the SAMPLE [Fig. 3(b)]. The elevation angle for both systems at this time was 2 deg above the horizon. The data in Fig. 3 are of relative backscatter intensity in decibels. These scans were collected at the same time during evening twilight. At that time, a shallow temperature inversion was likely to have recently started forming very near the surface with neutral stability above. Winds were from the northwest. The backscatter fields shown in Fig. 3 were computed by standard lidar processing procedures such as computing and subtracting the mean background from every record in each scan, correcting for the inverse-square law, and converting to decibels. Effects of extinction are not corrected. The images show three aerosol plumes that are moving across the sector area. They are moving from the NW to the SE. We do not know the specific source of these plumes, but they are likely the result of agricultural activities such as the operation of heavy equipment. The images are very
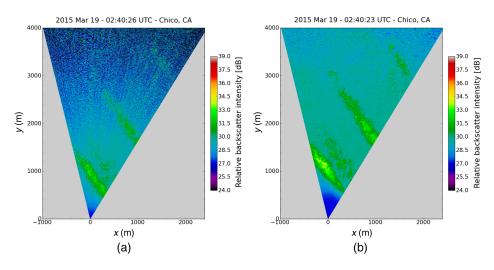
Fig. 3 (a) One unfiltered PPI scan of relative aerosol backscatter intensity from the REAL. (b) The same from the SAMPLE.

similar. However, differences include the appearance of stronger signal at far ranges in the SAMPLE image, more fine-scale detail at close ranges in the REAL image, and radial streaks in the REAL image that are associated with pulse-to-pulse variations in transmitted laser energy.

Figure 4 shows raw backscatter intensity as a function of range resulting from one pulse of the REAL and the closest possible 0.1 s integration of SAMPLE backscatter photon counts. These arrays came from the same scans as shown in Fig. 3 (at ~20-deg azimuth). Several significant characteristics can be noted. First, it is evident that the REAL detector was not optimally placed at the focus of the backscattered radiation, particularly in the along-axis (z) dimension. This means the overlap function is less than 1 at long ranges (the detector is not collecting all of the transmitted beam at longer ranges). It was not terribly off, but it explains why the REAL has higher signal at the near ranges and why the roll-off, or decay, in scattering intensity is steeper than SAMPLE. Second, the REAL waveform (blue) exhibits larger-amplitude, high-frequency random noise. The main sources of this noise comes from the excess noise factor of the APD and from the amplifier. Third, the region between 0 and 600 m is where the transmitted laser beam
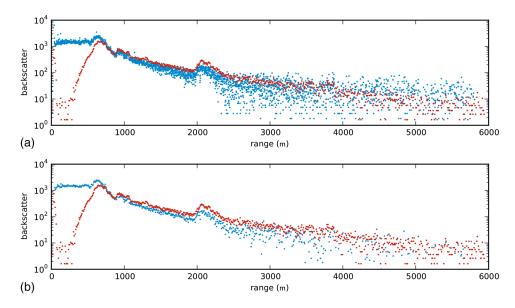

Fig. 4 Raw backscatter waveforms from the REAL and SAMPLE after subtraction of background mean. The REAL waveform (blue) resulted from one laser pulse. The SAMPLE waveform (red) resulted from the integration of 1500 laser pulses during a 0.1 s interval. (a) The native REAL resolution (1.5 m range gate) and (b) a 5-point binning to match SAMPLE resolution.

and the receiver FOV are not completely overlapped. This comes from defocused receiver light overfilling the detector (which acts as the field stop) in the REAL and the biaxial geometry of the SAMPLE.

4.1 Comparison of Raw Signal-to-Noise Ratio

Raw signal-to-noise ratio (SNR) is the SNR of the backscatter intensity data before any processing is performed. Raw SNR is computed by dividing the backscatter signal amplitude $I_0(r, \theta)$ at each gate in range by the standard deviation of the backscatter background σ_θ for that radial array. Here, r is the range and θ is the angle. The background is simply a subset of data points from the waveforms shown in Fig. 4 that are representative of incident power on the detector when backscatter is not present. The safest place to compute statistics of the background is from a set of data points just prior to the laser discharge (0 m range). Alternatively, data points near the long-range end of the waveform (e.g., to the right of 5000 m in Fig. 4) may be used if they are clear of backscatter signal from aerosol, clouds, and hard targets. We note that $I_0(r, \theta)$ is the backscatter waveform after the mean background has been subtracted

$$\mathrm{SNR}_{\mathrm{raw}}(r, \theta) = \frac{I_0(r, \theta)}{\sigma_\theta}. \tag{1}$$

Figure 5 shows the results of the calculation for the pair of waveforms shown in Fig. 4. Comparisons such as the one shown in Figs. 4 and 5 were performed for a variety of pointing angles and background conditions, although not shown here for brevity. The most impressive result was when the raw SNR of the SAMPLE was 6 to 10 times larger than that of the REAL during twilight conditions such as those shown. By binning the REAL data, the raw SNR of the SAMPLE was still 3 to 6 times larger than that of the REAL during those conditions. However, as the background radiation intensity increased the SAMPLE raw SNR decreased. For example, while scanning toward the north at noon, the SAMPLE raw SNR was only 1 to 2 times larger than that of the REAL. Binning the REAL data from the noon comparison resulted in slightly higher SNR for the REAL. We hypothesize that the background level depends on the position of the sun, the pointing direction of the lidar, and the presence and position of clouds and particulate matter that may scatter and absorb solar radiation.
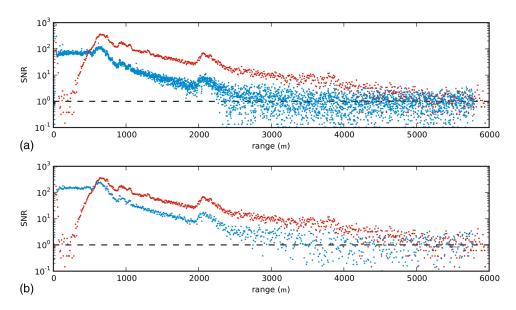

Fig. 5 Comparison of raw SNR. Blue data points are the result of one pulse of the REAL and the red data points are the result of a 0.1 s integration of photon counts for the SAMPLE. (a) The native REAL resolution (1.5 m range gate) and (b) a 5-point binning to match SAMPLE resolution.

4.2 *Comparison of Image Signal-to-Noise*

A goal of our work is to remotely sense two-component vector wind fields and aerosol plume motion using motion estimation algorithms. A critical step for motion estimation is high-pass median filtering in order to remove large-scale features from the images. The high-pass filter is applied in the radial dimension. In this work, we used a 500-m window to remove radially oriented features larger than 250 m. This corresponds to a 333-point filter for REAL and 67-point filter for SAMPLE. Backscatter data after applying these filters are shown in Figs. 6 and 7.

For the motion estimation algorithms to be successful, sufficient raw SNR is not the only requirement. In addition, the images must contain coherent aerosol features. There are times, typically during the night, when very few features are present within the scan domain, and other situations where features exist but are dominated by the random noise—especially in the far range. It is therefore important to detect the presence of aerosol features in order to discard irrelevant data. This is achieved using a quantity that we call "image-SNR" (iSNR).[20] iSNR is defined as the ratio of the local standard deviation of spatially coherent relative backscatter signal $\sigma_I(r, \theta)$ to the local standard deviation of noise $\sigma_\varepsilon(r, \theta)$. These local standard deviations are estimated from the autocorrelation function of the high-pass median filtered backscatter data, along the radial dimension (see Fig. 8). In this work, a window length of $\approx$280 m was used, that is 256 points for REAL and 32 points for SAMPLE data.

Coherent aerosol features correspond to larger values of iSNR. A simple thresholding can be applied to discriminate between features and irrelevant data—see an example of a scan by SAMPLE in Fig. 9. During this study, it was found that the low-pass median filter, applied to the backscatter along the radial direction in order to remove small hard-target outliers, has a deep influence on the iSNR. This is due to the fact that the low-pass median filter
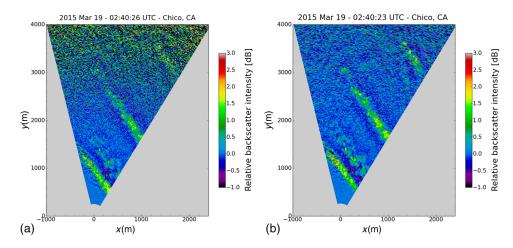

Fig. 6 (a) One high-pass median filtered PPI scan from the REAL. (b) The same from the SAMPLE. No low-pass median filtering was applied.
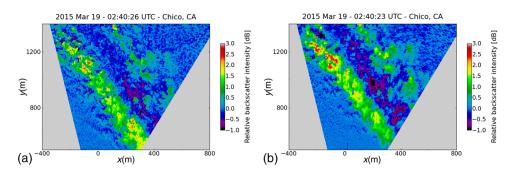

Fig. 7 (a) Zoomed-in region from one high-pass median filtered PPI scan from the REAL. (b) The same from the SAMPLE.
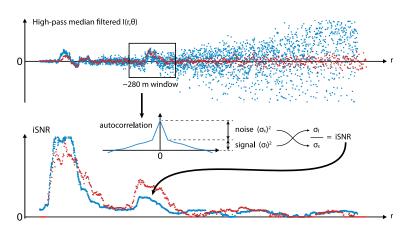
Fig. 8 Diagram showing how iSNR is calculated with actual data. Blue data points are from the REAL and red data points are from the SAMPLE. A gliding 280-m window (square on top graph) is applied to each high-pass median filtered radial array. Autocorrelation functions (middle sketch) and iSNR (bottom graph) are computed for all window positions.
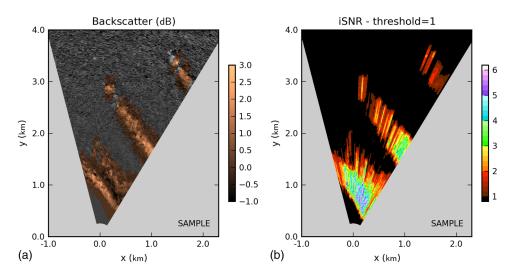

Fig. 9 Example of iSNR-based masking of irrelevant data for a SAMPLE scan. (a) The copper-colored aerosol features correspond to (b) an iSNR > 1, while noisy and/or feature-less data are shown in gray shades.

acts as a denoiser and thus increases the iSNR, as shown in Fig. 10. Without low-pass filtering, the iSNR from the SAMPLE is better than the REAL's beyond the range of ~900 m (top row). A low-pass filtering of the backscatter using a 22-m window (15 points for the REAL, 3 points for SAMPLE) highly reduces the noise and increases REAL's iSNR (bottom panel), in particular in the midrange. A bump in the iSNR corresponding to an aerosol plume appears progressively between 3 and 4 km, while it was previously buried in the noise. A direct consequence of this analysis is that the threshold value used to discriminate between coherent features and irrelevant data (Fig. 9) has to be adapted to the size of the low-pass filter. While low-pass filtering can significantly denoise data from the REAL and increase the iSNR, it also destroys some of the fine-scale structures. Thus, a trade-off must be found between the amount of denoising and the scales to be preserved.

4.3 Comparison of Wind Data

The wind estimation was performed at the end of the experiment on March 18 to 20, 2015.[21] Both instruments performed 45-deg sector scans covering [−15,30]-deg azimuth at 2-deg
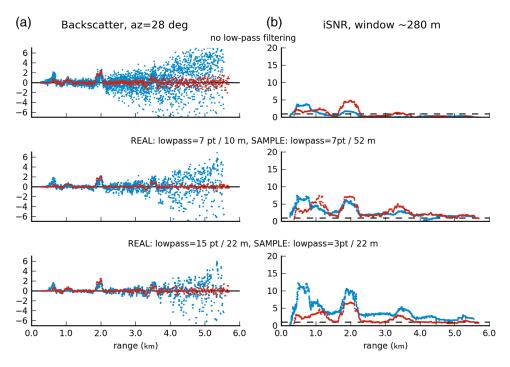
Fig. 10 Effects of the low-pass filter on (a) the backscatter and (b) iSNR on a backscatter profile of REAL (red) and SAMPLE (blue) data. Low-pass filtering significantly reduces the noise on data from the REAL and increases the iSNR (bottom row), especially in the midrange.

elevation in about 13 s for the REAL and 12 s for SAMPLE. Wind estimates were retrieved from both instruments using the two motion estimation algorithms that were previously validated on the REAL against an independent Doppler lidar: cross-correlation (software named Gale)[19] and wavelet-based optical flow (software named Typhoon).[20]

At the time of the side-by-side experiment, SAMPLE was not capable of quickly returning the telescope pointing direction to the starting angle of each scan, a move employed by the REAL beam steering unit and referred to as "fly-back." As a result, the SAMPLE swept the lidar beam back and forth in azimuth at the same rate while the REAL collected data only when scanning in one azimuthal direction and in between quick fly-backs. Therefore, for the purpose of motion estimation, SAMPLE had the disadvantage of having to skip every other scan in order to obtain the same time-step between two consecutive samples at any given location of the scan domain. Thus, the actual interscan time-step for SAMPLE data is 24 s while it was 14 s for the REAL. This limited our ability to compare directly REAL and SAMPLE wind estimates since larger time-steps result in larger velocity errors and the influence of the scan update rate cannot be separated from other parameters such as the radial resolution or sensitivity to noise.

Figure 11 shows an example of two-component horizontal vector wind fields estimated by both instruments approximately at the same time. Each vector field is superimposed over the first scan of the pair used for the motion estimation. Both the aerosol features, in the background, and the vector fields look very similar. The lack of vectors in some locations for the SAMPLE [Fig. 11(b)] is due to the slightly different masking strategies for each instrument (Sec. 4.2 and Fig. 9).

Figure 12 presents time-series of wind speed and direction measured on March 18 by both instruments using the wavelet-based optical flow algorithm, Typhoon. These values are extracted from the wind fields in a 50-m radius area located at 1.5-km range and 15-deg azimuth. Except for a few spurious estimates, both series are in very good agreement. Figure 13 shows time series measured on March 20 from SAMPLE data by both estimation methods. Values were extracted from the same location as with the series of Fig. 12. Again, both series are in very good agreement. Time series data such as these have previously been compared with wind measurements from Doppler lidar.[20]
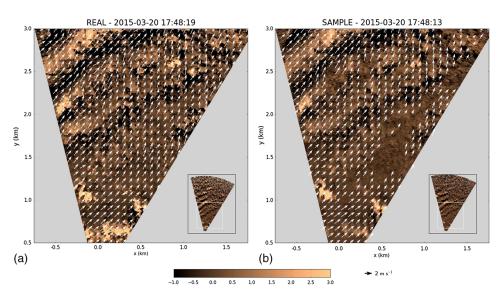
Fig. 11 Example of wind fields estimated by the wavelet-based optical flow algorithm from (a) REAL and (b) SAMPLE data on March 20, 2015, in Chico, California. Copper-shaded background is the high-pass median filtered aerosol backscatter intensity of the first scan of the pair used to retrieve each wind field. The corresponding time lapse animations span the period from 16:30:34 to 17:07:49 UTC (Video 1, MP4, 50.2 MB) [URL: http://dx.doi.org/10.1117/1.JRS.10 .016031.1].
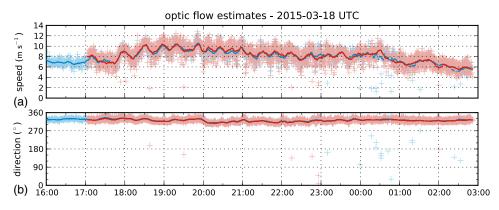

Fig. 12 Comparison of (a) wind speed and (b) direction measured by the wavelet-based optical flow for a point at 1.5-km range, 15-deg azimuth from the instruments. Blue data points are from REAL and red data points are from SAMPLE. "+" markers are instantaneous measures and continuous lines are 10-min rolling averages.

5 Offshore Winds

A particularly important and challenging environment to observe and simulate is that of the turbulent atmosphere over rough ocean surfaces.[22,23] Atmospheric simulations over oceans are challenging because, unlike terrain, the fluid bottom boundary moves vertically, and it does so quickly. Observations are challenging because of the difficulty of placing sensors near large amplitude and breaking waves in the open ocean especially during high wind conditions. The SAMPLE was transported to the northern California coast and deployed on various beaches there from March 21 to 31, 2015. The goal of the 10-day pilot experiment was to determine whether a compact micropulse lidar like the SAMPLE could be used to observe spray from breaking waves and estimate the wind field over rough ocean surfaces. The Pacific Ocean along the northern California coast is notoriously rough but unfortunately the weather conditions were such that we only observed high-amplitude sea states (2.4 to 3.6 m) on the last day of the experiment. Scanner fly-back capability that was lacking for the side-by-side comparison experiment in Chico was added and utilized during this deployment.
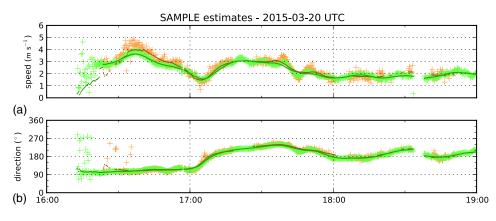
Fig. 13 Comparison of (a) wind speed and (b) direction measured from SAMPLE data for a point at 1.5-km range, 15-deg azimuth from the instruments. Orange data points are from the wavelet-based optical flow and green data points are from the cross-correlation. "+" markers are instantaneous measures and continuous lines are 10-min rolling averages.

For the work on the coast, the SAMPLE was deployed from the same U-Haul moving van used in Chico and powered by a small gasoline generator. The van was parked at public parking lots within meters of the beach and the ocean. Set-up and tear-down after each observation period typically took 1 h. The SAMPLE scanned mostly horizontally to observe the aerosol and wind field just above the ocean and occasionally vertically to reveal mixing in the vertical and marine boundary layer structure. The horizontal scans were just meters above the crests of the waves. Figure 14 shows SAMPLE observations in a sector scan that was collected in the early evening of March 30 (3:30 UTC on March 31) at Big Lagoon County Park (11.5 km north of Trinidad, California) when no whitecaps were observed beyond the surf zone. The bright plume structure along the right edge of the sector scan is the result of ocean waves breaking along the beach. The surf zone in this case served as a line source of particulate matter. The motion estimation algorithms were able to derive the offshore wind fields advecting these coherent plume structures to more than 1 km offshore. Shortly after this sequence of PPI scans, we collected vertical cross
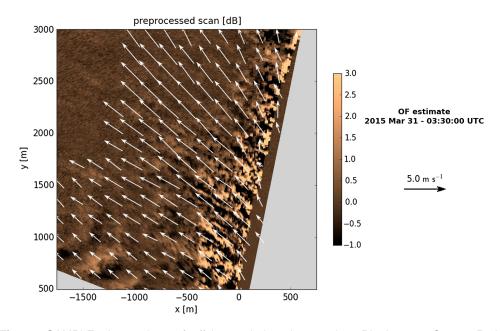

Fig. 14 SAMPLE observations of offshore wind and aerosol at Big Lagoon County Park, California, on the evening of March 30, 2015. The plumes of particulate matter were generated by breaking waves along the beach (near right side of sector scan area) and enable the determination of the offshore flow field. Vectors were calculated by the wavelet-based optical flow algorithm, Typhoon (Video 2, MP4, 10.8 MB) [URL: http://dx.doi.org/10.1117/1.JRS.10.016031.2].
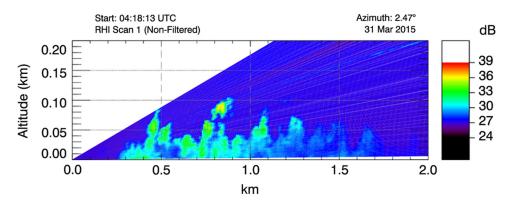
Fig. 15 RHI scan from the SAMPLE on March 31, 2015, at 4:18 UTC revealing particulate matter raised by turbulent flow above breaking ocean waves (Video 3, MP4, 563 KB) [URL: http://dx.doi .org/10.1117/1.JRS.10.016031.3].

sections (known as range-height indicator or RHI scans) obliquely through the surf zone (see Fig. 15). The RHI scans reveal plumes of particulate matter originating from the surf zone and being lofted by turbulence to altitudes of about 100 m. These data prove that the SAMPLE can detect sufficient aerosol intensity from breaking waves and that the plume structure can be used to determine flow fields.

The data shown in Fig. 16 were collected during the afternoon of the subsequent day from a deployment location in Samoa, California, that is 41 km south of Big Lagoon County Park. A synoptic scale cold front had passed over the region between the two observation periods resulting in a dramatic shift in the wind. The wind was from the northwest and the wave amplitude of the ocean was much larger than the previous evening. The elastic backscatter field [Fig. 16(a)] shows narrow and elongated aerosol plume structures that resemble streaks[24] typically observed in model output of neutral-stability shear-driven flows.[22] Visibility during the 31st was high and white caps beyond the surf zone were very sparse and fleeting. Therefore, this period would have been challenging for any lidar. Because of the weak aerosol backscatter signal intensity, we used the Gale algorithm to retrieve the vector fields shown in Fig. 16(b). We expect that if more whitecaps had been present, the aerosol structure would have been more pronounced and the wind field retrievals better.
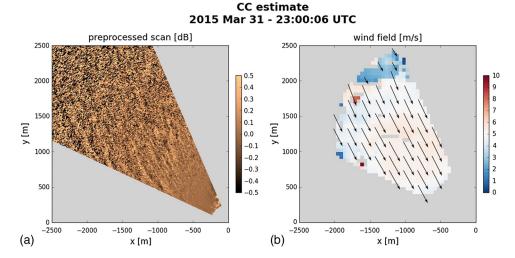

Fig. 16 SAMPLE observations of wind and aerosol from Samoa, California, on March 31, 2015, during a period with 2.4 to 3.6 m amplitude waves and wind from the NW. (a) High-pass median filtered backscatter showing aerosol that is organized into streaks that are elongated in the streamwise direction. (b) Wind field resulting from the cross-correlation algorithm, Gale. Despite the large ocean swells during this time, whitecaps were sparse and fleeting beyond the surf zone (Video 4, MP4, 25 MB) [URL: http://dx.doi.org/10.1117/1.JRS.10.016031.4].

6 Discussion and Conclusion

While the raw SNR of the SAMPLE data may be greater than that of the untouched REAL data (Fig. 5), subjective visual inspections of the imagery (such as Fig. 7) suggest that the REAL reveals more fine-scale detail in the radial dimension. For some applications, such as observing microscale gravity waves,[25] this detail is very valuable. However, for other applications, such as the estimation of wind fields, its value is questionable. This is because while the distance between samples in range remains constant with range, the distance between samples in the azimuthal direction increases with range. This fact is an unavoidable artifact of the polar coordinate system in which scanning lidar data are collected. Therefore, the high radial resolution of the REAL may be valuable to motion estimation in short ranges where the azimuthal resolution may be comparable to the radial resolution. However, at far ranges the detail is likely to be of no value in the motion estimation since there are no closely spaced neighboring arrays to sample that fine-scale structure in a subsequent scan.

The first main conclusion of our experiment and analysis of data is that the size, weight, and complexity of the REAL appear to be avoidable in future designs and that a path exists for wind field measurements from a dramatically more compact and efficient system. Currently, the major advantages of the REAL are: (1) continuous all-weather operation (due to the housing and beam steering unit); (2) immunity from second-trip echoes—which is significant when working in terrain and near clouds; (3) insensitivity to background radiation levels; and (4) high range resolution. The major disadvantages of the REAL are mostly due to the transmitter that results in high levels of required maintenance, power consumption, and waste heat generation. It also requires a large and stable operating environment. In addition, the small APD used in the REAL makes focusing the backscatter radiation a challenge. The major advantages of the SAMPLE are: (1) deployed size ($\sim$1.4 m^3) and weight ($\sim$450 lbs or 204 kg) and (2) improved performance in terms of backscatter SNR. A significant advantage of the SAMPLE also is the power consumption: only 850 W. The major disadvantage of the SAMPLE is the second trip echoes. The reduced range resolution from that of the REAL appears to be only a minor disadvantage. Finally, we note that the Hamamatsu detector employed in SAMPLE was special in that it had 10% quantum efficiency. The specification for the standard model is 2% and those with 10% are rare. The uncertain availability and high cost of PMTs at this wavelength with 10% quantum efficiency is also a disadvantage. Lowering the pulse rate of the laser (to avoid second trip echoes) while maintaining or increasing the pulse energy and spectral purity would be very advantageous.

The second important conclusion of our work is that breaking ocean waves do produce sufficient amounts of particulate matter for a micropulse lidar like the SAMPLE to detect and use as input to motion estimation algorithms. In the future, we would like to develop and apply a theoretical model to facilitate comparison and prediction of the performance of either style system (macropulse versus micropulse). Such a model would enable us to assess the merits of various system design trades. For example, to reduce the susceptibility to second trip echoes on a micropulse system, the pulse repetition frequency could be reduced to 10 kHz (or less). Doing so however would also reduce the average transmit power to 66% (or less) of the current value. However, such a performance reduction might be compensated for by adding a narrower interference filter or temperature-controlled etalon to provide better rejection of background radiation. Use of larger diameter telescopes is another possibility to increase performance, but with larger collection area comes larger background radiation. Again, a model is needed to quantitatively assess the impact of the various design options. The model would benefit from being validated by a long duration experiment whereby a SAMPLE and a REAL would be operated for long periods (at least several months, preferably a year or more), under a wide variety of weather and background radiation conditions.

In terms of packaging, a shared telescope as described by Spuler et al.[8] could eliminate the current biaxial design of SAMPLE and may result in an overall reduction in size, weight, and cost. In terms of configurations for enabling more atmospheric research, we expect greatly improved versatility from future designs. For example, a SAMPLE could easily be placed in a modest enclosure and pointed vertically from within the enclosure to utilize the scanning capability of a roof-top beam steering unit and the protection of a secure, weatherproof enclosure. Such a configuration would enable continuous, long-term operations. The instrument could also be

easily removed from the weatherproof enclosure and shipped for rapid deployments from various platforms.

Acknowledgments

References

1. V. Banakh and I. Smalikho, *Coherent Doppler Wind Lidars in a Turbulent Atmosphere*, Artech House, Boston (2013).
2. V. A. Kovalev and W. E. Eichinger, *Elastic Lidar: Theory, Practice, and Analysis Methods*, John Wiley and Sons, Hoboken (2004).
3. B. M. Gentry and C. L. Korb, "Edge technique for high-accuracy Doppler velocimetry," *Appl. Opt.* **33**(24), 5770–5777 (1994).
4. S. C. Tucker et al., "Optical autocovariance wind lidar (OAWL): aircraft test-flight history and current plans," *Proc. SPIE* **9612**, 96120E (2015).
5. R. K. Newsom et al., "Simultaneous analog and photon counting detection for Raman lidar," *Appl. Opt.* **48**, 3903–3914 (2009).
6. Y. Zhang et al., "Slope characterization in combining analog and photon count data from atmospheric lidar measurements," *Appl. Opt.* **53**, 7312–7320 (2014).
7. I. Razenkov, "Characterization of a Geiger-mode avalanche photodiode detector for high special resolution lidar," Master's Thesis, University of Wisconsin—Madison, Madison, Wisconsin (2010).
8. S. M. Spuler et al., "Field-deployable diode-laser-based differential absorption lidar (dial) for profiling water vapor," *Atmos. Meas. Tech.* **8**(3), 1073–1087 (2015).
9. J. D. Spinhirne, "Micro pulse lidar," *IEEE Trans. Geosci. Remote Sens.* **31**, 48–55 (1993).
10. S. D. Mayor and E. W. Eloranta, "Two-dimensional vector wind fields from volume imaging lidar data," *J. Appl. Meteor.* **40**, 1331–1346 (2001).
11. S. D. Mayor et al., "Comparison of aerosol backscatter and wind field estimates from REAL and SAMPLE," *Proc. SPIE* **9612**, 96120G (2015).
12. S. D. Mayor and S. M. Spuler, "Raman-shifted eye-safe aerosol lidar," *Appl. Opt.* **43**, 3915–3924 (2004).
13. S. M. Spuler and S. D. Mayor, "Scanning eye-safe elastic backscatter lidar at 1.54 microns," *J. Atmos. Oceanic Technol.* **22**, 696–703 (2005).
14. S. D. Mayor et al., "Polarization lidar at 1.54-microns and observations of plumes from aerosol generators," *Opt. Eng.* **46**, 096201 (2007).
15. S. M. Spuler and S. D. Mayor, "Raman shifter optimized for lidar at 1.5-micron wavelength," *Appl. Opt.* **46**, 2990–2995 (2007).
16. S. D. Mayor et al., "Recent improvements to the Raman-shifted eye-safe aerosol lidar (real)," *Proc. SPIE* **8872**, 88720B (2013).
17. S. D. Mayor et al., "Lidars: a key component of urban biodefense," *Biosecur. Bioterror.* **6**, 45–56 (2008).
18. S. D. Mayor, J. P. Lowe, and C. F. Mauzey, "Two-component horizontal aerosol motion vectors in the atmospheric surface layer from a cross-correlation algorithm applied to scanning elastic backscatter lidar data," *J. Atmos. Oceanic Technol.* **29**, 1585–1602 (2012).
19. M. Hamada et al., "Optimization of the cross-correlation algorithm for two-component wind field estimation from single aerosol lidar data and comparison with Doppler lidar," *J. Atmos. Oceanic Technol.* **33**, 81–101 (2016).
20. P. Dérian, C. F. Mauzey, and S. D. Mayor, "Wavelet-based optical flow for two-component wind field estimation from single aerosol lidar data," *J. Atmos. Oceanic Technol.* **32**, 1759–1778 (2015).

21. S. D. Mayor et al., "Two-component wind fields from single scanning aerosol lidar," *Proc. SPIE* **9612**, 96120D (2015).
22. P. P. Sullivan, J. C. McWilliams, and E. G. Patton, "Large-eddy simulation of martine atmospheric boundary layers above a spectrum of moving waves," *J. Atmos. Sci.* **71**, 4001–4027 (2014).
23. S. D. Mayor et al., "Observations of two-component wind fields from aerosol lidar and motion estimation algorithms including first results over rough sea states," in *Int. Conf. on Model Integration across Disparate Scales in Complex Turbulent Flow Simulation*, p. 28 (2015).
24. P. Drobinski and R. Foster, "On the origin of near-surface streaks in the neutrally-stratified planetary boundary layer," *Bound. Layer Meteorol.* **108**(2), 247–256 (2003).
25. T. N. Randall, "Observations of microscale gravity waves in the nocturnal boundary layer above an orchard canopy by a horizontally scanning lidar," Master's Thesis, California State University Chico (2015).

Shane D. Mayor is an assistant professor at California State University Chico. His PhD is in atmospheric and oceanic sciences from the University of Wisconsin–Madison. His research interests include atmospheric lidar and microscale and boundary layer meteorology. He is a member of SPIE.

Pierre Dérian is a postdoctoral researcher at the Inria Rennes—Bretagne Atlantique, France. He received his PhD in applied mathematics at the University of Rennes 1, France. His research interests include image processing, motion estimation, and numerical modeling and simulation in connection with fluid dynamics and geosciences.

Christopher F. Mauzey is a research associate in the Atmospheric Lidar Research Group at California State University Chico. He received his BS degree in computer science from California State University Chico in 2010. His role in the research group is software development and system administration. He specializes in parallel computing on graphics processors.

Scott M. Spuler is a research engineer at the National Center for Atmospheric Research. He received his MS and PhD degrees in applied optics/engineering systems from Colorado School of Mines in 1999 and 2001, respectively. His research interests include the development of innovative optical and laser-based instrument systems that can be applied to enhance the understanding of the atmosphere.

Patrick Ponsardin is an optical scientist at Spectral Sensor Solutions, LLC. He received his MS degree in applied physics from Paris Diderot University and a diploma of advanced studies in optics from Pierre and Marie Curie University in Paris. His current research interests are in the development and application of aerosol lidars for the detection of plumes of biological origin and the development and application of standoff Raman sensors for the detection of surface contaminants.

Jeff Pruitt is a remote sensing scientist at the Harris Corporation and holds a BS in physics from Kansas State University. His experience in lidar includes wind monitoring, airborne CO_2 measurements, and chem/bio cloud identification and tracking. He holds six patents in the field of active remote sensing.

Darrell Ramsey is a senior engineer at National Security Technologies, LLC, and has an MS degree in electrical engineering from the University of Arizona as well as a BS degree in electrical engineering from New Mexico State University. His technical specialties are electro-optical systems, lidar, and high-speed fiber optic-based data acquisition systems.

Noah S. Higdon is the president of Spectral Sensor Solutions, LLC, an electro-optical remote sensing R&D company. He has an MS degree in optical sciences from the University of Arizona and has spent over 37 years designing, developing, and applying lidar technology for atmospheric research, environmental monitoring, and chemical–biological threat sensing. He is a member of SPIE.